

Local density of states in two-dimensional topological superconductors under a magnetic field: signature of an exterior Majorana bound state

Shu-Ichiro Suzuki, Yuki Kawaguchi, and Yukio Tanaka
Department of Applied Physics, Nagoya University, Nagoya, 464-8603, Japan
 (Dated: April 9, 2018)

We study quasiparticle states on a surface of a topological insulator (TI) with proximity-induced superconductivity under an external magnetic field. An applied magnetic field creates two Majorana bound states: a vortex Majorana state localized inside a vortex core and an exterior Majorana state localized along a circle centered at the vortex core. We calculate the spin-resolved local density of states (LDOS) and demonstrate that the shrinking of the radius of the exterior Majorana state, predicted in Ref. [R. S. Akzyanov *et al.*, Phys. Rev. B **94**, 125428 (2016)], under a strong magnetic field can be seen in LDOS without smeared out by non-zero-energy states. The spin-resolved LDOS further reveals that the spin of the exterior Majorana state is strongly polarized. Accordingly, the induced odd-frequency spin-triplet pairs are found to be spin-polarized as well. In order to detect the exterior Majorana states, however, the Fermi energy should be closed to the Dirac point to avoid contributions from continuum levels. We also study a different two-dimensional topological-superconducting system where a two-dimensional electron gas with the spin-orbit coupling is sandwiched between an *s*-wave superconductor and a ferromagnetic insulator. We show that the radius of an exterior Majorana state can be tuned by an applied magnetic field. However, on the contrary to the results at a TI surface, neither the exterior Majorana state nor the induced odd-frequency spin-triplet pairs are spin-polarized. We conclude that the spin-polarization of the Majorana state is attributed to the spin-polarized Landau level which is characteristic for systems with the Dirac-like dispersion.

I. INTRODUCTION

The existence of edge states is one of the most characteristic properties of topological phases. The edge states stem from the topology of bulk wavefunctions, and have been actively studied in this decade¹⁻⁴. In particular, exploring Majorana bound states (MBSs) in topological superconductors (TSCs) is of great worth^{3,5-18}, since topologically protected quantum computation can be implemented by braiding MBSs^{19,20}. The presence of MBSs in condensed matters has first been proposed in spinless *p*-wave superconductors (SCs)^{5,21}. Majorana bound states have been considered to be observed by means of current fluctuations⁷ and tunneling spectroscopy^{9,15,16}. Recently, more accessible experimental setups have been proposed in various hybrid systems where a spin-singlet *s*-wave SC is proximity-coupled to a low-dimensional semiconductor with a strong spin-orbit coupling²²⁻²⁹. Several experimental studies found the evidences of MBSs³⁰⁻⁴⁴.

Among these hybrid systems, SCs on a three-dimensional topological insulator (TI) are promising systems to observe and manipulate MBSs⁴⁵⁻⁵². In such systems, a MBS appears as a localized state at a vortex core⁵³⁻⁵⁶. Simultaneously, another MBS should appear somewhere in the system because MBSs can appear only in pairs¹¹. Recently, R. S. Akzyanov *et al.* have shown the existence of exterior MBSs which are not always pinned by an interface nor a sample edge^{57,58}. Focusing only on the zero-energy solutions, they have concluded that the position of the exterior MBS can be controlled by an applied magnetic field⁵⁸. From experimental side, on the other hand, the local conductance

measurements by STS has become accessible in this hybrid system⁵⁹. Therefore, the study on the quasiparticle energy spectrum, including the exterior MBS, non-zero-energy Andreev bound states, and the continuum levels, is indispensable to observing MBSs and realizing the braiding MBSs. Motivated by these works, in this paper, we investigate how one can identify the existence of the exterior MBS and its position shift dependent on an applied magnetic field from the local density of state (LDOS) experiment.

Another aspect of physics of MBSs is the appearance of odd-frequency Cooper pairs. In general, Cooper pairs are classified into several symmetry classes by focusing on the symmetry of the anomalous Green's function. Most theoretical papers have focused only on the equal-

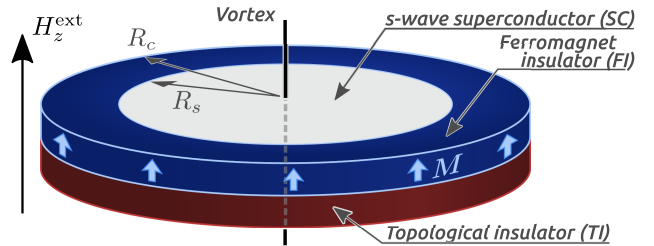


FIG. 1. Schematic of superconductor (SC)/topological insulator (TI) hybrid system. A superconducting island with a single vortex is fabricated on the top of a TI. The SC is surrounded by a ferromagnetic insulator (FI) to bound the quasiparticles. Therefore, the magnetization of the FI is perpendicular to the TI surface and its magnitude is much larger than the chemical potential and the pair potential.

time pairing, of which the anomalous Green's functions are even-function of the relative time of two fermions. However, the anomalous Green's function depends generally on the relative time (i.e., frequency), and can be an odd function of the frequency. Such odd-frequency Cooper pairs are known to be locally induced by spatial inhomogeneity as subdominant components^{60–75}. Majorana bound states are equivalent to zero-energy Andreev bound states², which always accompany subdominant odd-frequency Cooper pairs. So far, the relation among odd-frequency pairing, MBSs, and TSCs have been studied in a number of works^{69,76–85}. The features of MBSs can be elucidated by focusing on the induced odd-frequency pairings. Therefore, it is worth investigating which type of Cooper pairs is induced by the novel exterior MBS.

In this paper, we study quasiparticle states on a TI surface where *s*-wave superconductivity is proximity-induced, which we refer to as the SC/TI hybrid system, and investigate how the LDOS is changed under an external magnetic field normal to the TI surface. Here, we put a vortex state of an even-frequency spin-singlet *s*-wave SC on the TI so that the vortex MBS and the exterior MBS arise. From the calculated LDOS, we numerically confirm that the wavefunction of the exterior MBS is localized on a circle around the vortex and the radius shrinks as the external magnetic field increases. In order to detect the exterior MBS from the LDOS, however, the Fermi energy should be set close to the Dirac point to avoid contributions from continuum levels. We also calculate the spin-resolved LDOS, and show that the exterior MBS is strongly spin-polarized. The direction of the spin polarization is determined by the direction of the external field. This property is related to the lowest “relativistic” Landau level^{86–88}, which is specific to systems with the Dirac-like dispersion such as TI surfaces. Accordingly, we find that odd-frequency spin-polarized *s*-wave Cooper pairs are accompanied by the exterior MBS.

We also study a different two-dimensional TSC known as the Rashba SC: a two-dimensional electron gas (2DEG) with a Rashba spin-orbit coupling (SOC) sandwiched between an *s*-wave SC and a ferromagnetic insulator (FI). We show that the position of the exterior MBS is tunable by an applied magnetic field as seen in SC/TI hybrid systems. However, contrary to the results in SC/TI hybrid systems, the exterior MBS is not spin polarized. This difference can be well interpreted by comparing the spin structure of the $n = 0$ Landau level. Reflecting that the $n = 0$ Landau level is not spin-polarized in a system with a conventional parabolic dispersion, the exterior MBS is not spin polarized in the Rashba SC.

The organization of this paper is as follows. In Sec. II, we present the Bogoliubov-de Gennes (BdG) Hamiltonian for the SC/TI hybrid system (Sec. II A) and the Rashba SC (Sec. II B) and the formulation to obtain the energy spectrum, LDOS, and pair amplitudes (Sec. II C). In Sec. III, we numerically calculate the energy spectrum, LDOS, and odd-frequency pairing both for SC/TI hybrid

systems and Rashba SCs. Section IV summarizes our results.

II. BOGOLIUBOV-DE GENNES FORMALISM

A. Superconductor/topological insulator hybrid system

We consider a surface of a three-dimensional TI on which a superconducting island is fabricated as shown in Fig. 1, where we use a type-II SC and a vortex is assumed to be located at the center of the SC. The SC is surrounded by an FI to bound quasiparticles at the SC/TI interface: The magnetization of the FI is directed perpendicular to the TI surface and its amplitude is much larger than the chemical potential and the pair potential so that a large energy gap opens at the FI/TI interface. The radii of the SC and the system are denoted by R_s and R_c , respectively. The existence of the FI is not essential when an exterior MBS is localized inside the superconducting region under a strong magnetic field. The FI is needed to localize an exterior MBS at the SC/FI boundary under a small magnetic field. Because a TI surface is already an interface between a 3DTI and a vacuum, we cannot terminate the metallic TI surface by a vacuum but need to introduce another type of insulating state by putting an FI on it. From the point of view of numerical calculations, the existence of the FI makes the boundary condition simple so that quasi-particle wavefunctions vanish at the boundary of the system.

When the superconductivity is induced by attaching a SC on the top of the TI, the system can be described by the Hamiltonian as

$$\mathcal{H} = \frac{1}{2} \iint \Psi^\dagger(\mathbf{r}) \tilde{H}_B(\mathbf{r}, \mathbf{r}') \Psi(\mathbf{r}') d\mathbf{r} d\mathbf{r}', \quad (1)$$

$$\Psi(\mathbf{r}) = [\psi_\uparrow(\mathbf{r}) \ \psi_\downarrow(\mathbf{r}) \ \psi_\uparrow^\dagger(\mathbf{r}) \ \psi_\downarrow^\dagger(\mathbf{r})]^T, \quad (2)$$

with the Bogoliubov-de Gennes (BdG) Hamiltonian

$$\tilde{H}_B(\mathbf{r}, \mathbf{r}') = \begin{bmatrix} \delta(\mathbf{r} - \mathbf{r}') \hat{h}(\mathbf{r}) & \hat{\Delta}(\mathbf{r}, \mathbf{r}') \\ -\hat{\Delta}^*(\mathbf{r}, \mathbf{r}') & -\delta(\mathbf{r} - \mathbf{r}') \hat{h}^*(\mathbf{r}) \end{bmatrix}, \quad (3)$$

where $\mathbf{r} = (x, y)$ and the symbol $\hat{(\cdot)}$ represents a 2×2 (4×4) matrix in the spin (spin-Nambu) space. The single-particle Hamiltonian \hat{h} and the pair potential $\hat{\Delta}$ can be written as

$$\hat{h}(\mathbf{r}) = v_F \hat{\boldsymbol{\sigma}} \cdot \left[\mathbf{p} - \frac{e}{c} \mathbf{A}(\mathbf{r}) \right] + M(\mathbf{r}) \hat{\sigma}_3 - \mu_F \hat{\sigma}_0, \quad (4)$$

$$\hat{\Delta}(\mathbf{r}, \mathbf{r}') = \delta(\mathbf{r} - \mathbf{r}') \Delta(\mathbf{r}) i \hat{\sigma}_2, \quad (5)$$

where v_F , $e < 0$, c , $\mathbf{p} = -i\hbar\nabla$, $\hat{\sigma}_i$ ($i = 0-3$), $\mathbf{A}(\mathbf{r})$, and μ_F are the Fermi velocity, the charge of an electron, the speed of light, the momentum operator, the Pauli matrices in the spin space, the vector potential, and the chemical potential, respectively. We here assume that the pair potential $\hat{\Delta}$ has the even-frequency spin-singlet *s*-wave

symmetry. The magnetization of the FI and the amplitude of the proximity-induced pair potential are denoted by $M(\mathbf{r})$ and $\Delta(\mathbf{r})$, respectively.

When the system is cylindrically symmetric, the Hamiltonian can further be reduced by introducing the cylindrical coordinate; $\mathbf{r} = (\rho, \phi)$. We assume that the ϕ dependence of the pair potential is written as $\Delta(\mathbf{r}) = \Delta(\rho)e^{-i\ell\phi}$ with ℓ being the vorticity and that the magnetization $M(\mathbf{r})$ does not depend on ϕ . Then, by expanding the field operators as $\Psi(\phi, \rho) = \sum_{\mu} \Psi_{\mu}(\rho)e^{i\mu\phi}/(2\pi)^{1/2}$ with the basis

$$\Psi_{\mu}(\rho) = \begin{pmatrix} \psi_{\uparrow, \mu}(\rho)e^{-i(\ell+1)\phi/2} \\ \psi_{\downarrow, \mu}(\rho)e^{-i(\ell-1)\phi/2} \\ \psi_{\uparrow, \mu}^{\dagger}(\rho)e^{+i(\ell+1)\phi/2} \\ \psi_{\downarrow, \mu}^{\dagger}(\rho)e^{+i(\ell-1)\phi/2} \end{pmatrix}, \quad (6)$$

where μ is an integer (a half integer) for an odd (even)

vorticity to make Ψ a single-valued function, the Hamiltonian is rewritten as

$$\mathcal{H} = \frac{1}{2} \sum_{\mu} \int_0^{R_c} \Psi_{\mu}^{\dagger}(\rho) \check{H}_{B, \mu}(\rho) \Psi_{\mu}(\rho) \rho d\rho, \quad (7)$$

$$\check{H}_{B, \mu}(\rho) = \begin{bmatrix} \hat{h}_{\mu}(\rho) & \Delta(\rho)i\hat{\sigma}_2 \\ -\Delta^*(\rho)i\hat{\sigma}_2 & -\hat{h}_{-\mu}^*(\rho) \end{bmatrix}. \quad (8)$$

The 4×4 Hamiltonian $\check{H}_{B, \mu}$ preserves the particle-hole symmetry

$$\check{H}_{B, \mu} = -\tilde{\tau}_1 \check{H}_{B, -\mu}^* \tilde{\tau}_1, \quad (9)$$

where $\tilde{\tau}_i$ ($i = 1-3$) are the Pauli matrices in the Nambu space. The single-particle Hamiltonian $\hat{h}_{\mu}(\rho)$ is given by

$$\hat{h}_{\mu}(\rho) = \begin{bmatrix} M(\rho) - \mu_F & \frac{\hbar v_F}{i} \left(\partial_{\rho} + \frac{2\mu - \ell + 1}{2\rho} + \tilde{A}_{\phi}(\rho) \right) \\ \frac{\hbar v_F}{i} \left(\partial_{\rho} - \frac{2\mu - \ell - 1}{2\rho} - \tilde{A}_{\phi}(\rho) \right) & -M(\rho) - \mu_F \end{bmatrix}. \quad (10)$$

Here, we chose the gauge $\mathbf{A}(\mathbf{r}) = A_{\phi}(\rho)\mathbf{e}_{\phi}$ with \mathbf{e}_{ϕ} being a unit vector along the azimuthal direction and defined $\tilde{A}_{\phi} = |e|A_{\phi}/\hbar c$. The vector potential is due to an external magnetic field in addition to the magnetic flux of a vortex. Throughout this paper, we assume that the thickness of the SC along the z direction is much thinner than its magnetic penetration depth so that the magnetic field is spatially homogeneous on the TI surface. The magnitude of an external magnetic field is expressed in terms of the magnetic length $\ell_B = (\hbar c/|eH_z^{\text{ext}}|)^{1/2}$, which should be larger than the coherence length $\xi_{\text{SC}} = \hbar v_F/\Delta_{\text{SC}}$ of the bulk SC with pair potential Δ_{SC} : otherwise, the magnetic field destroys the superconductivity. On the other hand, ξ_{SC} is much smaller than the coherence length $\xi_0 = \hbar v_F/\Delta_0$ of the proximity-induced pair potential Δ_0 on the TI surface (i.e., $\Delta_0 \ll \Delta_{\text{SC}}$). In the following calculations, we consider the case for $\xi_{\text{SC}} \ll \xi_0 < \ell_B$.

To describe the ρ dependence around the vortex core, we assume

$$\Delta(\rho) = \Theta(R_s - \rho) \Delta_0 \tanh(\rho/\xi_0), \quad (11)$$

where R_s is the radius of the SC, Δ_0 is the amplitude of the proximity-induced pair potential in the absence of a vortex, and $\Theta(\rho)$ is the Heaviside step function. The radial profile of the magnetization is given by $M(\rho) = M_0\Theta(\rho - R_s)\Theta(R_c - \rho)$ with R_c being the outer radius of the FI.

B. Rashba superconductor

We also consider a 2DEG with a Rashba SOC. The 2DEG is sandwiched between an even-frequency spin-singlet s -wave SC and an FI, where a superconducting vortex is located at the center of the SC and the magnetization of the FI is normal to the 2DEG as shown in Fig. 2. In this paper, we refer to this system as the Rashba SC. Both of the two systems (Figs. 1 and 2) are two-dimensional islands of a topological superconductor surrounded by an insulating state even though the geometries look different. The appearances are different from each other because FIs play different roles; an FI is introduced to make an insulating region in the SC/TI hybrid system, whereas it is introduced to make a superconductivity topological in the Rashba SC.

The single-particle Hamiltonian for the Rashba SC can be described^{22,24-28} as

$$\hat{h} = \left[\frac{\tilde{\mathbf{p}}^2}{2m_0} - \mu_F \right] \hat{\sigma}_0 + \lambda \mathbf{e}_z \cdot [\hat{\boldsymbol{\sigma}} \times \tilde{\mathbf{p}}] + \mathbf{M} \cdot \hat{\boldsymbol{\sigma}}, \quad (12)$$

where λ is the strength of the SOC, $\tilde{\mathbf{p}} = \mathbf{p} - (e/c)\mathbf{A}$, \mathbf{e}_z is the unit vector in the z -direction, m_0 is the mass of an electron. In the Cartesian coordinate, \hat{h} can be written

as

$$\hat{h}(x, y) = \begin{bmatrix} \xi_k + M_0 & \lambda(\tilde{\partial}_x - i\tilde{\partial}_y) \\ \lambda(-\tilde{\partial}_x - i\tilde{\partial}_y) & \xi_k - M_0 \end{bmatrix}, \quad (13)$$

where we have used $\mathbf{M} = M_0 \mathbf{e}_z$ with M_0 being a constant, $\xi_k = (-\hbar^2/2m_0)(\tilde{\partial}_x^2 + \tilde{\partial}_y^2) - \mu_F$ and $\tilde{\partial}_{x(y)} = \partial_{x(y)} + i|e|A_{x(y)}/\hbar c$. The system becomes topologically non-trivial (i.e., the 2DEG becomes a TSC) when the relation $M_0^2 > \mu_F^2 + \Delta_0^2$ is satisfied^{22–25,28}.

Similarly to the previous section, the Hamiltonian can be simplified when the system has the rota-

tional symmetry. Assuming $\Delta(\rho, \phi) = \Delta(\rho)e^{-i\ell\phi} = \Delta_0 \tanh(\rho/\xi_0)e^{-i\ell\phi}$ and expanding the field operators as Eq. (6), the Hamiltonian can be written as

$$\mathcal{H} = \frac{1}{2} \sum_{\mu} \int_0^{R_c} \Psi_{\mu}^{\dagger}(\rho) \check{H}_{B,\mu}(\rho) \Psi_{\mu}(\rho) \rho d\rho, \quad (14)$$

$$\check{H}_{B,\mu}(\rho) = \begin{bmatrix} \hat{h}_{\mu}(\rho) & \Delta(\rho)i\hat{\sigma}_2 \\ -\Delta^*(\rho)i\hat{\sigma}_2 & -\hat{h}_{-\mu}^*(\rho) \end{bmatrix}, \quad (15)$$

where the diagonal part is given by

$$\hat{h}_{\mu}(\rho) = \begin{bmatrix} \xi_{\mu} + M_0 & \lambda \left(\partial_{\rho} + \frac{2\mu - \ell + 1}{2\rho} + \tilde{A}_{\phi} \right) \\ \lambda \left(-\partial_{\rho} + \frac{2\mu - \ell - 1}{2\rho} + \tilde{A}_{\phi} \right) & \xi_{\mu+1} - M_0 \end{bmatrix}, \quad (16)$$

with

$$\xi_{\mu} = -\frac{\hbar^2}{2m_0} \left[\frac{1}{\rho} \frac{\partial}{\partial \rho} \left(\rho \frac{\partial}{\partial \rho} \right) - \frac{(2\mu - \ell - 1)^2}{4\rho^2} + \frac{\tilde{A}_{\phi}(2\mu - \ell - 1)}{2\rho} - |\tilde{A}_{\phi}|^2 \right] - \mu_F, \quad (17)$$

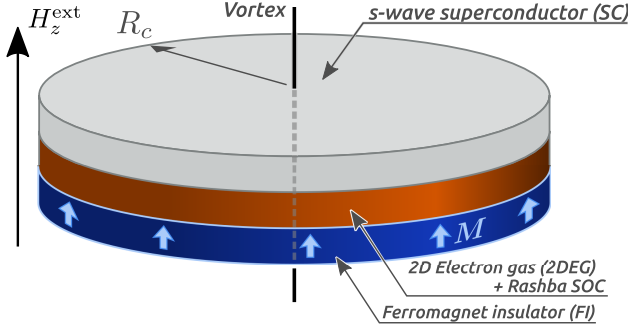


FIG. 2. Schematic of Rashba SC system. The two-dimensional electron gas (2DEG) is sandwiched between an FI and an s -wave SC with a vortex. The magnetization of the FI is normal to the 2DEG.

being the kinetic energy in the cylindrical coordinate. The definition of \tilde{A}_{ϕ} is the same as that in Sec. II A. $\check{H}_{B,\mu}$ in Eq. (15) also preserves the particle-hole symmetry described in Eq. (9).

C. Local density of states and pair amplitudes

The local density of states (LDOS) and the pair amplitudes can be calculated from the quasiparticle eigen-

functions. We numerically solve the BdG equation

$$H_{B,\mu} \Phi_{\mu,\nu} = E_{\mu,\nu} \Phi_{\mu,\nu}, \quad (18)$$

for each μ , and obtain the eigenfunctions $\Phi_{\mu,\nu} = [u_{\uparrow,\mu,\nu} \ u_{\downarrow,\mu,\nu} \ v_{\uparrow,\mu,\nu} \ v_{\downarrow,\mu,\nu}]^T$ where $u_{s,\mu,\nu}$ and $v_{s,\mu,\nu}$ are the wavefunctions of quasiparticles in spin $s = \uparrow$ and \downarrow states and μ and ν are the indices that specify the ϕ dependence of the wavefunction and the eigenvalue, respectively. In the numerical simulations, we expand the eigenfunction in terms of the Bessel functions and numerically diagonalize the BdG Hamiltonian. The details are described in Appendices A (SC/TI hybrid system) and B (Rashba SC).

Using the eigenfunctions, the LDOS is expressed as

$$N(\rho, E) = \sum_{s=\uparrow,\downarrow} N_s(\rho, E), \quad (19)$$

$$N_s(\rho, E) = \sum_{\mu} \sum_{E_{\mu,\nu} \geq 0} [|u_{s,\mu,\nu}(\rho)|^2 \eta(E - E_{\mu,\nu}) + |v_{s,\mu,\nu}(\rho)|^2 \eta(E + E_{\mu,\nu})]. \quad (20)$$

In this paper, we employ the thermal-smearing function $\eta(E) = -(\partial/\partial E)f(E, T)$, where $f(E, T)$ is the Fermi-Dirac distribution function. The temperature is set to $T = 0.1T_c$ for the SC/TI hybrid systems and $T = 0.01T_c$ for the Rashba SCs, where the critical temperature T_c is obtained from the relation between T_c and Δ_0 in an s -wave singlet superconductor: $T_c = \Delta_0 e^{\gamma}/\pi$, where γ is Euler's gamma.

We can obtain the anomalous Green's function from the eigenfunctions as well. Throughout this paper, we refer to the anomalous Green's function as a pair amplitude. In general, for a given set of eigenfunctions $[u_{\uparrow,\nu} \ u_{\downarrow,\nu} \ v_{\uparrow,\nu} \ v_{\downarrow,\nu}]^T$ and associated eigenvalues E_ν , the anomalous Green's function is given by

$$\begin{aligned} \mathfrak{F}_{\sigma_1\sigma_2}(i\omega_n; \mathbf{r}_1, \mathbf{r}_2) &= \sum_{E_\nu \geq 0} \left[\frac{u_{\sigma_1,\nu}(\mathbf{r}_1) v_{\sigma_2,\nu}^*(\mathbf{r}_2)}{i\omega_n - E_\nu} + \frac{v_{\sigma_1,\nu}^*(\mathbf{r}_1) u_{\sigma_2,\nu}(\mathbf{r}_2)}{i\omega_n + E_\nu} \right], \end{aligned} \quad (21)$$

where $\omega_n = (2n+1)\pi T$ is the Matsubara frequency with n being an integer. In the present case, by recovering the ϕ dependence of the quasiparticle wavefunctions using Eq. (6), the anomalous Green's function can be expressed as

$$\begin{aligned} \mathfrak{F}_{s_1s_2}(i\omega_n; \mathbf{r}_1, \mathbf{r}_2) &= \sum_{\mu} \mathfrak{F}_{\mu,s_1s_2}(i\omega_n; \mathbf{r}_1, \mathbf{r}_2), \quad (22) \\ \mathfrak{F}_{\mu,s_1s_2}(i\omega_n; \mathbf{r}_1, \mathbf{r}_2) &= \sum_{E_\nu \geq 0} \left[\frac{u_{s_1,\mu,\nu}(\rho_1) v_{s_2,\mu,\nu}^*(\rho_2)}{i\omega_n - E_{\mu,\nu}} e^{+i\mu\phi_r} + \frac{v_{s_1,\mu,\nu}^*(\rho_1) u_{s_2,\mu,\nu}(\rho_2)}{i\omega_n + E_{\mu,\nu}} e^{-i\mu\phi_r} \right] \\ &\quad \times e^{-i\ell\phi_c} e^{-i(X_{s_1}\phi_1 + X_{s_2}\phi_2)/2}, \end{aligned} \quad (23)$$

with $\phi_c = (\phi_1 + \phi_2)/2$, $\phi_r = \phi_1 - \phi_2$, and $X_s = 1(-1)$ for $s = \uparrow(\downarrow)$. In this paper we focus on the s -wave component (i.e., on-site correlation function). We can obtain the even- and odd-frequency components from the following relation:

$$\begin{aligned} F_{\mu,s_1s_2}^{\text{Even(Odd)}}(i\omega_n; \rho_1, \phi_1) &= \frac{1}{2} \left[\mathfrak{F}_{\mu,s_1s_2}(i\omega_n; \rho_1, \phi_1, \rho_1, \phi_1) + (-) \mathfrak{F}_{\mu,s_1s_2}(-i\omega_n; \rho_1, \phi_1, \rho_1, \phi_1) \right]. \end{aligned} \quad (24)$$

III. RESULTS

A. Superconductor/topological insulator hybrid system

1. Local density of states

We first show the LDOS with several choices of the magnetic length in Fig. 3, where the chemical potential is set to $\mu_F = 0.2\Delta_0$. The LDOS $N(\rho, E)$ in this system is normalized by $N_0 = \bar{N}(\rho = 0, E = 1.5\Delta_0)$ for each chemical potential, where $\bar{N}(\rho, E)$ is the LDOS of the

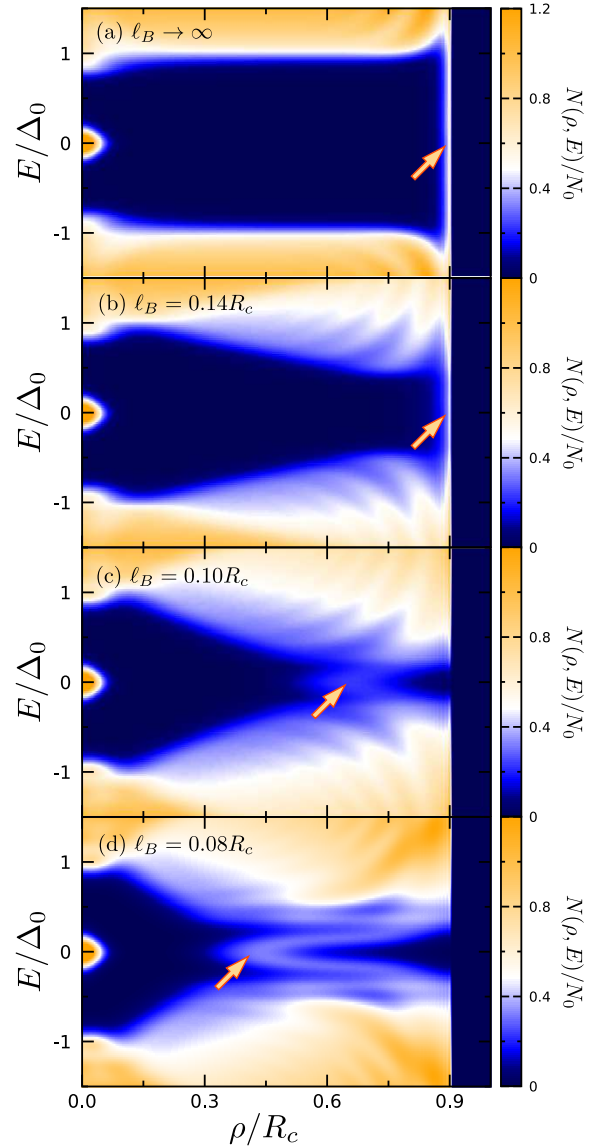


FIG. 3. Local density of states (LDOS) in the SC/TI hybrid system. The vortex is located at the center of the superconducting island $\rho = 0$. The peaks at $\rho = E = 0$ are from the vortex Majorana bound states (MBS). The exterior MBS changes its position depending on an external magnetic field (indicated with the arrows). The V-shape peaks near the arrows in (c) and (d) are the characteristic structure for the exterior and chiral MBSs. The LDOS are normalized by the value at $\rho = 0$ and $E = 1.5\Delta_0$ in the absence of the proximity-induced pair potential (i.e., $\Delta_0 = 0$). The parameters are set as $\mu_F = 0.2\Delta_0$, $R_c = 30\xi_0$, $R_s = 0.9R_c$, $\ell = 1$, and $M_0 = 10\Delta_0$.

pristine surface of the TI in the absence of a proximity-induced pair potential nor an external magnetic field. In the absence of an external magnetic field (i.e., $\ell_B \rightarrow \infty$), the proximity-induced pair potential opens a spatially-homogeneous energy gap almost everywhere in the superconducting region [Fig. 3(a)]. A vortex MBS appears

at the center of the vortex core at $E = 0$. The peaks at $\rho = 0$ and $E = \pm 0.95\Delta_0$ are also the localized states at the vortex core. The exterior of the superconducting region (i.e., $\rho > R_s$) is insulating because of the magnetization of the FI. As a result, another MBS⁸⁹ appears at the SC/FI boundary (i.e., $\rho = R_s$).

With decreasing the magnetic length, the magnitude of the superconducting gap near the SC/FI boundary decreases as shown in Fig. 3(b). When the magnetic length becomes shorter than a certain value, the MBS at the SC/FI boundary moves inside the superconducting region. In Figs. 3(c) and 3(d), for example, the zero-energy peaks are located at $\rho \approx 0.7R_c$ and $0.4R_c$, respectively. The radius of the exterior MBS r^* becomes smaller for larger magnetic field and is consistent with the relation $r^* = 2\ell_B^2/\xi_0$ derived in Ref. 58.

In addition to the zero-energy states, there are also subgap “edge” states with non-zero eigenenergies. These states, known as chiral Majorana states, stem from the solutions for $\mu \neq 0$ and exhibits linear dispersion with respect to μ for small μ (see Fig. 6). They are localized at the SC/FI boundary when $H_z^{\text{ext}} = 0$. When H_z^{ext} becomes stronger than a certain value, they move inside the superconducting region as the exterior Majorana zero-energy state does. The radii of these states depend on their eigenenergies: the higher-energy state, or equivalently the larger-angular-momentum state, has the larger radius. As a result, the LDOS exhibits a characteristic V-shaped peak in the ρ - E space as shown in Figs. 3(c) and 3(d). The chiral Majorana states exist even in the absence of a superconducting vortex, although the exactly-zero-energy state arises only in the presence of a vortex^{9,12}. We observe numerically that the chiral Majorana states without a vortex also move inside the superconducting region under a strong external magnetic field.

We next show the LDOS for a larger chemical potential $\mu_F = 0.4\Delta_0$ (i.e., with a larger Fermi surface). In the absence of an external magnetic field, the magnitude of the energy gap is equivalent to Δ_0 except for the vortex core and the boundary as shown in Fig. 4(a). When the magnetic field is applied, the energy gap becomes smaller around the SC/FI boundary as shown in Fig. 4(b). At the magnetic length $\ell_B = 0.1R_c$ and $0.08R_c$, $N(E = 0, \rho)$ has a peak at $\rho \approx 0.7R_c$ and $0.4R_c$, respectively. However, these points are saddle points in the ρ - E plane (i.e., these points are local minima along the E direction). Accordingly, the characteristic V-shape structure in the ρ - E space, which can be seen in Fig.3(d), is segmented at $E = 0$ in Fig. 4(d).

To understand the details of the LDOS for each chemical potential, we plot the cross section of $N(\rho, E)$ for $\mu_F = 0.2\Delta_0$ and $0.4\Delta_0$ in Figs. 5(a) and 5(b), respectively. The radial coordinate is fixed at $\rho/R_c = 0.35, 0.40, 0.45$, and 0.50 (i.e., around the zero-energy peak of the exterior MBSs). When the chemical potential is sufficiently small, the LDOS has a clear peak at $E = 0$ as shown in Fig. 5(a). However, when $\mu_F = 0.4\Delta_0$, there

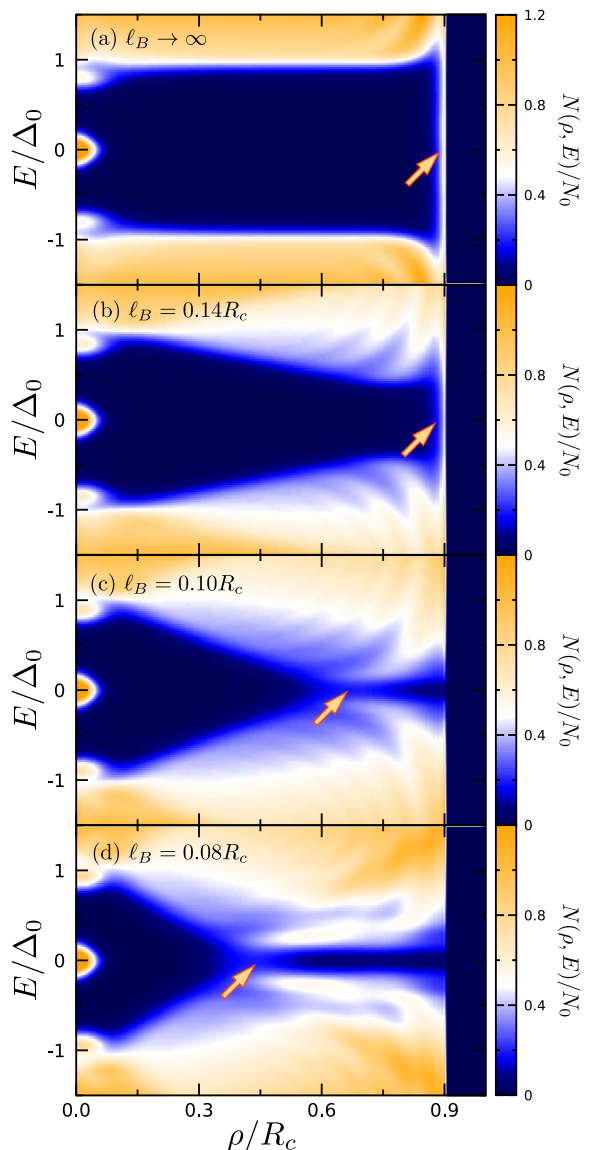


FIG. 4. LDOS in the SC/TI hybrid system at $\mu_F = 0.4\Delta_0$. The other parameters are set as the same values as those used in Fig. 3. The arrows indicate the position of the exterior Majorana bound states. The characteristic V-shape is no longer clear.

is no zero-energy peak for every ρ even though there is an exterior MBS.

Figure 6 shows the angular-momentum dependences of the energy eigenvalues at $\ell_B = 0.08R_c$ and (a) $\mu_F/\Delta_0 = 0.2$, (b) 0.4 , and (c) 2.0 . In Fig. 6(a), one can clearly identify the chiral Majorana mode, which goes across the figure from the bottom left to the top right. In the absence of an external field, the chiral Majorana mode has a linear dispersion in the wide range of μ (not shown) and its dispersion is given by $E_{\text{CM}} \sim \mu \text{sgn}[M_0]$. Namely, the direction of the magnetization in the FI determines the direction of the edge current⁴⁷.

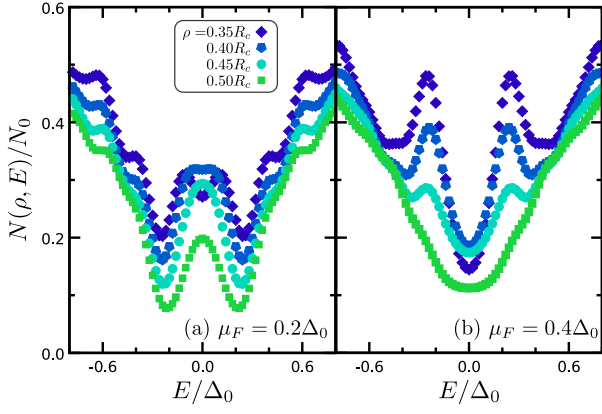


FIG. 5. LDOS in the SC/TI hybrid system. The same data as (a) Fig. 3(d) and (b) Fig. 4(d), which are respectively calculated for $\mu_F = 0.2\Delta_0$ and $0.4\Delta_0$, are shown as a function of E/Δ_0 at $\rho/R_c = 0.35, 0.40, 0.45$, and 0.50 . When the chemical potential μ_F is close to the Dirac point (a), the exterior Majorana state can be observed as a zero-energy conductance peak. On the other hand, LDOS for a fixed ρ has a minimum at $E = 0$ when μ_F is not sufficiently small (b).

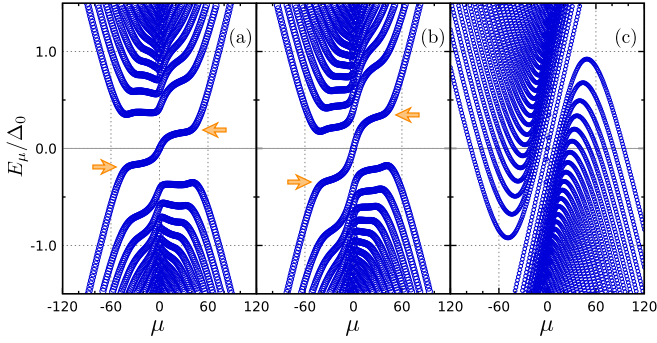


FIG. 6. Angular momentum dependences of the energy spectrum for the chemical potential (a) $\mu_F = 0.2\Delta_0$, (b) $0.4\Delta_0$, and (c) $2.0\Delta_0$. The magnetic length is set to $\ell_B = 0.08R_c$. The plateaus emerge in the presence of an external field. In particular, the chiral Majorana bound state includes the $n = 0$ Landau level, which is indicated with arrows in the panels (a) and (b).

An external magnetic field modifies the energy spectrum through the emergence of the Landau quantizations^{86–88}. In the energy spectrum, almost-flat plateaus corresponding to the Landau levels of the normal state emerge (indicated with arrows in Fig. 6). These Landau levels are given by $E = E_{\pm, n}^R \equiv \pm \hbar v_F \sqrt{2n}/\ell_B - \mu_F$ and $E = -E_{\pm, n}^R$ for particle and hole branches, respectively, where the particle (hole) branches arise for $\mu < 0$ ($\mu > 0$) when $H_z^{\text{ext}} > 0$. We note that the $\pm E_{n=0}^R$ plateaus emerge in a chiral Majorana mode (see Appendix C for details). However, the linear dispersion with respect to μ remains at around $\mu = 0$. The sign of the slope around $\mu = 0$ is determined by the direction of

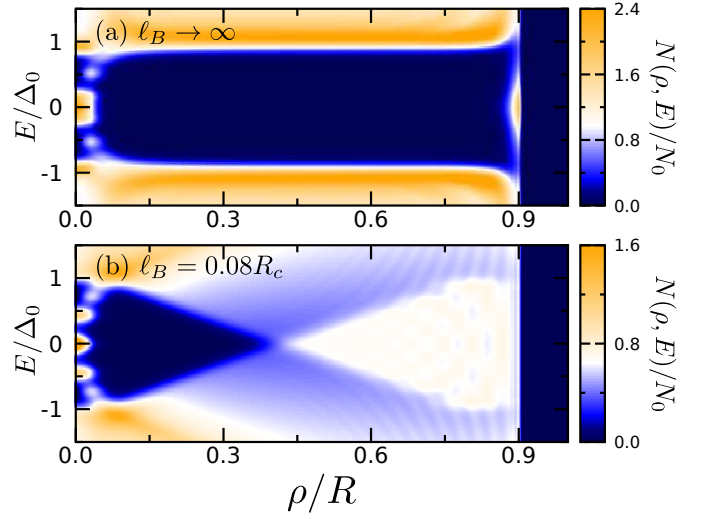


FIG. 7. LDOS in the SC/TI hybrid system at $\mu_F = 2.0\Delta_0$. The other parameters are set as the same values as those used in Fig. 3. When the chemical potential μ_F is not sufficiently small, the exterior Majorana state is clearly seen only in the absence of an external magnetic field is shown in (a). Under an external field, the contributions from the continuum states smear out the peak from the exterior Majorana state as shown in (b).

an applied magnetic field H_z^{ext} . These dispersive states make the characteristic V-shape peak in the ρ - E space.

The position where the exterior MBS appears is an effective boundary between a TSC and a topologically trivial material. Applying a strong magnetic field (i.e., $\ell_B < R_s$), a TI becomes gapped even in the normal state due to the Landau quantization. Introducing an s -wave pair potential, Landau levels in the energy range $|E_{\pm, n}^R| \leq \Delta_0$ open a superconducting energy gap, and contributes a topological superconductivity. The radius of the topological superconducting region, in this case, depends on ℓ_B because ℓ_B determines the radius the Landau orbit and the energy of the Landau level. As a result, the region with $\rho < r^*$ becomes a TSC, whereas that with $\rho > r^*$ does not become a TSC but remains to be a normal (non-topological) insulator. Although there is no actual boundary such as interfaces, there is a “boundary” on the radius r^* at which an exterior MBS appears.

The Landau quantization also modifies the continuum levels. For the same magnetic field, the shift of the continuum states becomes more significant for a larger chemical potential [Fig. 6(c)]. As the chemical potential increases, the plateaus corresponding to the $n = 1$ states approach to the Fermi level. At large enough chemical potential (e.g., $\mu_F = 2.0\Delta_0$), the energy gap between the continuum states completely disappears as shown in Fig. 6(c). The contributions from the continuum states smear out the peak from the exterior MBS in LDOS. The LDOS for $\mu_F = 2.0\Delta_0$ are shown in Fig. 7. The two zero-

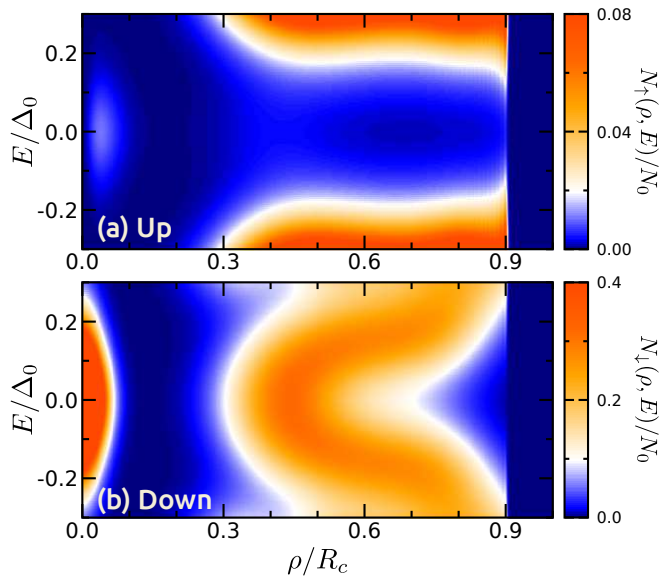


FIG. 8. Spin-resolved LDOS (a) N_{\uparrow} and (b) N_{\downarrow} in the SC/TI hybrid system at $\mu_F = 0.2\Delta_0$ and $\ell_B = 0.08R_c$. The other parameters are set as the same values as those used in Fig. 3. The amplitude of N_{\downarrow} is much larger than that of N_{\uparrow} at the place where the exterior and vortex Majorana states appear, meaning that these Majorana bound states are spin-polarized.

TABLE I. Dependence of the majority spins of the vortex and exterior Majorana states on the external-field direction and the vorticity.

H_z^{ext}	ℓ	Vortex MBS	Exterior MBS
+	+1	Down	Down
-	+1	Down	Up
+	-1	Up	Down
-	-1	Up	Up

energy states at the vortex core and the SC/FI boundary can be clearly seen when $\ell_B \rightarrow \infty$ [Fig. 7(a)], whereas the exterior mode cannot be identified when $\ell_B = 0.08R_c$ because the energy gap is closed in the region of $\rho > 0.4R_c$ [Fig. 7(b)]. We have confirmed that the exterior MBS is located at $\rho = 0.85R_c$ in this magnetic field. Namely, when the chemical potential is too large, it is difficult to observe the exterior MBS through a zero-energy peak even though its position can be controlled by an applied field. Hence, we need to set the chemical potential close to the Dirac point in order to avoid contribution from non-zero-energy states⁹⁰. We also carry out the same simulations for larger systems such as $R_c = 150\xi_0$, and confirm that the above conclusion does not change qualitatively.

Next, we discuss the spin structure of the MBSs. The spin-resolved LDOS for the up-spin N_{\uparrow} and for down-spin

N_{\downarrow} are shown in Fig. 8, where we set $\mu_F = 0.2\Delta_0$ and $\ell_B = 0.08R_c$. As shown in Fig. 8, the exterior MBS is strongly polarized. The LDOS for the down spin N_{\downarrow} has a zero-energy peak around $\rho = 0.4R_c$ and exhibits the characteristic V-shaped peak structure in the ρ - E space. On the other hand, the amplitude of N_{\uparrow} at the same place is totally small. In the case of a TI surface, the wavefunctions for the $n = 0$ Landau level are fully spin polarized (see Appendix C for details). Correspondingly, the chiral Majorana mode which is constituted from the $n = 0$ Landau levels are spin polarized as well⁹¹.

The majority spin of the exterior MBS is determined by $\text{sgn}[H_z^{\text{ext}}]$ because the direction of the spin polarization for the $n = 0$ Landau level is determined by $\text{sgn}[H_z^{\text{ext}}]$. Additionally, the vortex MBS is also strongly spin polarized. As shown in Fig. 8, the height of the peak around $\rho \simeq 0.05R_c$ in N_{\uparrow} is much smaller than the peak at $\rho = 0$ in N_{\downarrow} . The majority spin of the vortex MBS is determined by the vorticity ℓ . This behavior is consistent with the previous discussions^{54,55,58}. The relation among the spin polarization of MBSs, the external magnetic field, and the vorticity is summarized in Table I.

2. Odd-frequency Cooper pairs

We discuss the correspondence between the MBSs and odd-frequency Cooper pairs. Superconducting phenomena near the Fermi level can be interpreted by two different physical descriptions: quasiparticle description and Cooper-pair description. Connecting these two descriptions, one can see that, when a MBS appears, odd-frequency Cooper pairs must appear behind it (see, for example, Ref. [69]). So far, phenomena related to odd-frequency Cooper pairs accompanied by vortex MBSs have been discussed^{65,66,68}. For example, the frequency symmetry of Cooper pairs can be clarified by means of the local Josephson coupling^{65,74}. Such results hold also for exterior MBSs.

We show the ρ -dependences of the anomalous Green's functions in Fig. 9, where we fix the center of the azimuthal angle $\phi_c = 0$ and $\mu_F = 0.2\Delta_0$, and the region attached to the FI is shaded. The magnetic length is set to (a) $\ell_B \rightarrow \infty$ and (b) $0.08R_c$. The imaginary (real) part of the even-frequency (odd-frequency) components are not shown because they are negligibly small in this scale of the plot. We show the magnified figures in the insets.

The results for $\ell_B \rightarrow \infty$ are shown in Fig. 9(a). The MBS appears at the SC/FI boundary as shown in Fig. 3. Correspondingly, the odd-frequency spin-triplet Cooper pairs appear there. Here, all of the triplet components (i.e., $F_{\uparrow\uparrow}^{\text{Odd}}$, $F_{\downarrow\uparrow+\uparrow\downarrow}^{\text{Odd}}$, and $F_{\downarrow\downarrow}^{\text{Odd}}$) have almost the same amplitudes at the SC/FI boundary, meaning that the synthetic spins of the odd-frequency Cooper pairs are not aligned. At the vortex core, there are peaks of the odd-frequency components^{65,66,68} corresponding to the vortex MBSs. In particular, $F_{\downarrow\downarrow}^{\text{Odd}}$ becomes nonzero even at

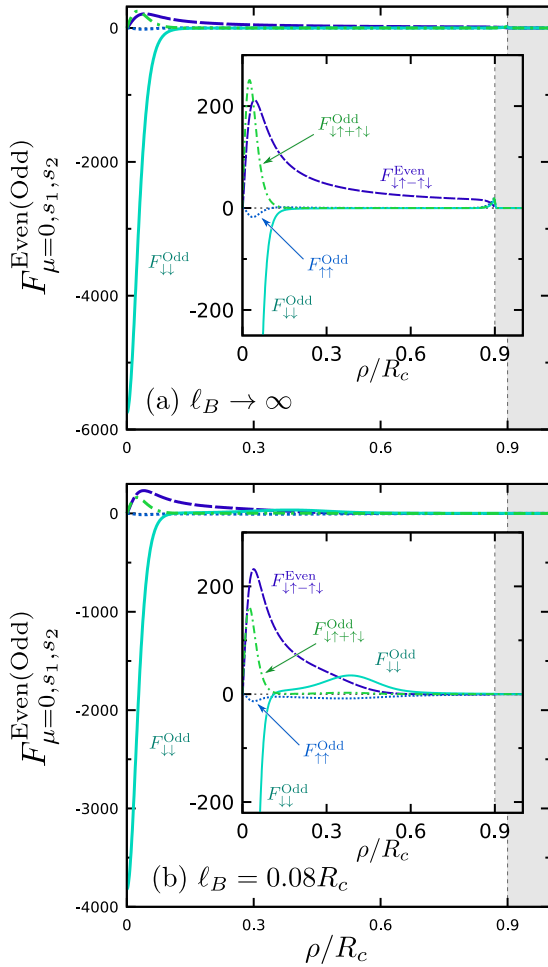


FIG. 9. Pair amplitudes in the SC/TI hybrid system with (a) $\ell_B \rightarrow \infty$ and (b) $\ell_B = 0.08R_c$. We show the magnified figures in the insets. Here only the contributions from $\mu = 0$ are shown because the Majorana states are the eigenfunctions for $\mu = 0$. The chemical potential and the Matsubara frequency are set to $\mu_F = 0.2\Delta_0$ and $\omega_n = 0.1\Delta_0$, respectively. The other parameters are the same as those used in Fig. 3. When $H^{\text{ext}} = 0$, the odd-frequency Cooper pairs are localized at the SC/FI boundary but not spin-polarized. When $H^{\text{ext}} \neq 0$, the odd-frequency pairs move into the superconducting region as the exterior Majorana state does. Simultaneously, the amplitude of $F_{\downarrow\downarrow}^{\text{Odd}}$ is much larger than those of $F_{\uparrow\uparrow}^{\text{Odd}}$ and $F_{\downarrow\uparrow\uparrow\downarrow}^{\text{Odd}}$ there. Namely, the odd-frequency pairs are spin-polarized, reflecting that the exterior Majorana state is spin-polarized.

$\rho = 0$. The conventional even-frequency pair amplitude is known to be suppressed at the place where Andreev bound states appear.^{65,66,68,70–72} We have confirmed that the spatial profile of $F_{\downarrow\uparrow\uparrow\downarrow}^{\text{Even}}$ for $\ell_B \rightarrow \infty$ becomes similar to $\Delta(\rho)$ given in Eq. (11) (i.e., $\Delta(\rho)$ is suppressed at around $\rho = 0$ and R_s , by summing up with respect to μ).

In the presence of an external magnetic field, the odd-frequency pairs at the SC/FI boundary move inside the superconducting region. At $\ell_B = 0.08R_c$, only the $F_{\downarrow\downarrow}^{\text{Odd}}$

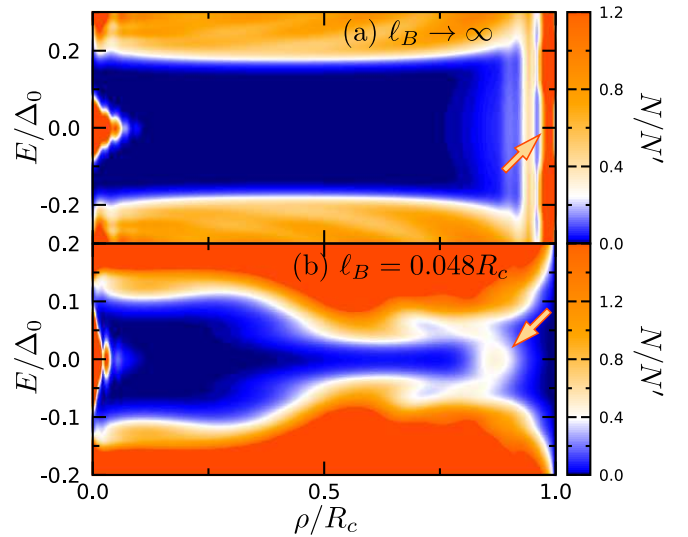


FIG. 10. LDOS in the Rashba SC at (a) $\ell_B \rightarrow \infty$ and (b) $\ell_B = 0.048R_c$. The edge of the SC is located at $\rho = R_c$. The results are normalized by N' , which is the LDOS at $E = 0.4\Delta_0$ and $\rho = 0.2R_c$ in the superconducting state without an external field. The parameters are set to $\mu_F = 0.2\mu_F$, $R_c = 180\xi_0$, $\ell = 1$, $M_0 = 1.2\Delta_0$, and $m_0\lambda^2 = \Delta_0$. The exterior Majorana state is located at the edge of the system in (a), whereas it moves to $\rho \approx 0.85R_c$ in (b). The arrows indicate the position of the exterior Majorana state.

component has a peak around $\rho \approx 0.4R_c$. This radius is exactly where the spin-polarized exterior MBS has a large amplitude. The direction of spin polarization of the odd-frequency pairs is determined by the spin polarization of the $n = 0$ “relativistic” Landau level⁸⁸ (i.e., determined by $\text{sgn}[H_z^{\text{ext}}]$). The place where the odd-frequency pair amplitude emerges is actually a boundary between a superconducting region and an insulating region due to the Landau quantization: Even though the superconducting pairing is proximity induced at $\rho < R_s$ from an external SC, the even-frequency pair amplitude is highly suppressed outside the region surrounded by the peak of the odd-frequency pair amplitude as shown in Fig. 9(b).

B. Rashba superconductor

The Rashba SCs can also host the MBSs at the vortex core and at the edge as in the case of the SC/TI hybrid system. We discuss the numerical results for the Rashba SC satisfying the topological criterion^{22–25,28} $M_0^2 > \mu_F^2 + \Delta_0^2$. We show the LDOS for $\ell_B \rightarrow \infty$ and $\ell_B = 0.048R_c$ in Figs. 10(a) and 10(b), respectively, where the parameters are set to $\mu_F = 0.2\Delta_0$, $R_c = 180\xi_0$, $m_0\lambda^2 = \Delta_0$, and $M_0 = 1.2\Delta_0$.

In the absence of an external field, the MBSs are located at the center of the core and at the edge of a system. These Majorana states appear as zero-energy peaks

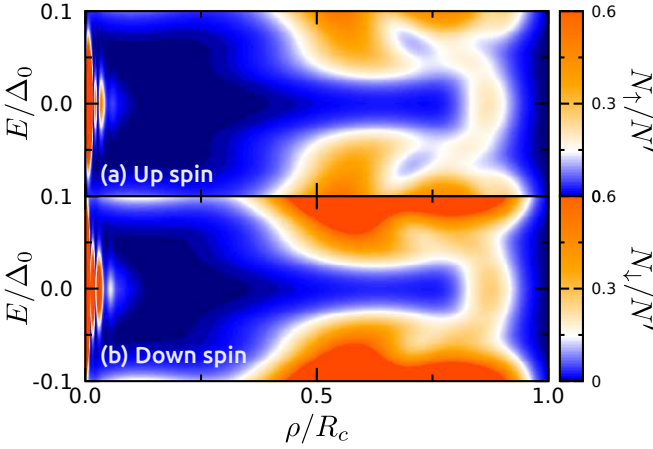


FIG. 11. Spin-resolved LDOS (a) N_{\uparrow} and (b) N_{\downarrow} in the Rashba SC at $\ell_B = 0.048R_c$. The edge of the SC is located at $\rho = R_c$. The results are normalized by N' defined in Fig. 10. The other parameters are the same as those used in Fig. 10. Contrary to the case in Fig. 8, the exterior Majorana state at $\rho = 0.85R_c$ consists of the up- and down-spin quasiparticles.

in LDOS at $\rho = 0$ and $\rho = R_c$. Here, the magnitude of the energy gap is smaller than Δ_0 because this energy gap is caused by the effective triplet pairings^{25,28}. The result in the presence of a magnetic field is shown in Fig. 10(b). The subgap states do not appear at the edge of the system but at $\rho \approx 0.85R_c$. Namely, by applying an external field, the exterior MBS for the Rashba SC moves inside a superconducting region as seen in an SC/TI hybrid system. We therefore conclude that the controllability of the exterior MBS is not restricted to materials with linear dispersion but a general property of two-dimensional TSCs.

However, there are two qualitative differences between exterior MBS in a Rashba SC and that in a SC/TI hybrid system. First, the exterior MBS is not spin-polarized as shown in Fig. 11, where the spin-resolved LDOS in a Rashba SC are plotted. Reflecting the quadratic dispersion, the wavefunction of the $n = 0$ Landau level is not spin-polarized in a Rashba SC (see Appendix C). As a result, the exterior MBS and the corresponding triplet odd-frequency Cooper pairs are not spin-polarized. The pair amplitudes are shown in Fig. 12. In the absence of an external magnetic field, the pair amplitudes have peaks at the edge of the system. When $\ell_B = 0.048R_c$, on the other hand, the peaks move inside the system as seen in the case of SC/TI hybrid systems. However, $F_{\uparrow\uparrow}^{\text{Odd}}$ and $F_{\downarrow\downarrow}^{\text{Odd}}$ have similar spatial profiles though their signs are opposite. In other words, the odd-frequency Cooper pairs are not spin polarized in a Rashba SC.

Second, the characteristic V-shape peak in the LDOS cannot be identified in Fig. 10(b). In a Rashba SC, a energy gap is smaller compared with that in an SC/TI hybrid system. As a result, there is only a few subgap “edge” states. Although one can increase the number of

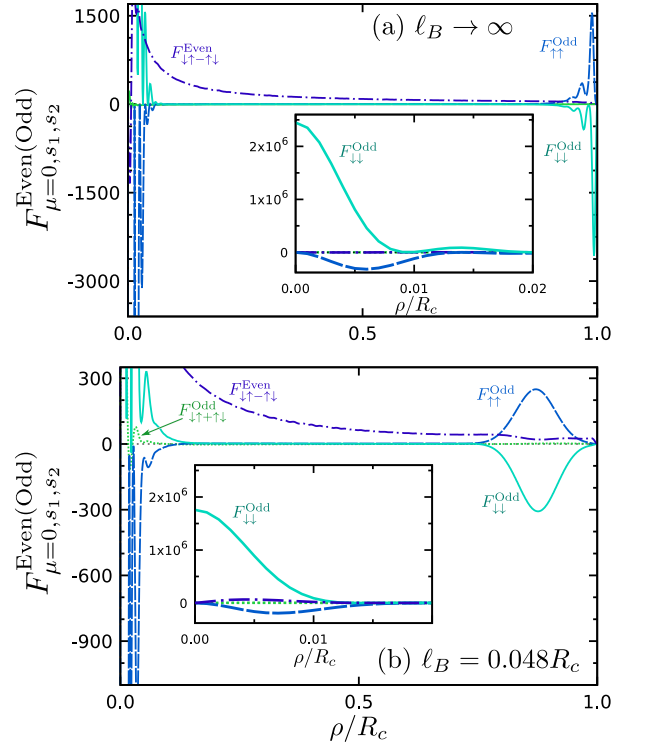


FIG. 12. Pair amplitudes in the Rashba SC at $\mu = 0$ with (a) $\ell_B \rightarrow \infty$ and (b) $\ell_B = 0.048R_c$. Here the results are shown with limited vertical axes to focus on the exterior Majorana state. The pair amplitudes near the vortex are shown in the insets. The Matsubara frequency are set to $\omega_n = 0.01\Delta_0$ which is smaller than the effective gap. The other parameters are the same as those used in Fig. 10. Reflecting that the exterior Majorana state is not spin-polarized in a Rashba SC, the odd-frequency Cooper pairs are not spin-polarized (i.e., $F_{\uparrow\uparrow}^{\text{Odd}}$ and $F_{\downarrow\downarrow}^{\text{Odd}}$ have almost the same amplitude).

subgap states by increasing a system size, in that case, the continuum states approach to the Fermi level in the presence of an external magnetic field, and smear out the exterior MBS. Accordingly in a Rashba SC, fine tunings of many parameters (e.g., radius of a Rashba SC and an external magnetic field) are required to observe the exterior MBS.

IV. CONCLUSION

We have theoretically studied the quasiparticle spectrum of two-dimensional topological superconductors hosting a vortex under an external magnetic field. We have mainly considered the surface of a topological insulator to which a superconductor with a superconducting vortex is proximity-coupled. We have obtained the spin-resolved local density of states by solving the Bogoliubov-de Gennes equation, and shown that the exterior Majorana state can be observed as a peak in the local density of states, which form a characteristic V-shaped peak in

radius-energy space. Carrying out the same simulations for a Rashba superconductor, we have concluded that the shift in the real space of the exterior Majorana state by applying a magnetic field is general property of two-dimensional topological superconductors.

Moreover, we have elucidated that there are qualitative difference between the exterior Majorana state in a topological-insulator surface and that in a Rashba superconductor. In the former case, an exterior Majorana state is fully spin polarized reflecting the spin-polarization of the $n = 0$ relativistic Landau level. On the other hand, in a Rashba superconductor, an exterior Majorana state is not spin polarized because of a conventional quadratic dispersion relation.

This difference affects on the spin structure of induced spin-triplet odd-frequency s -wave Cooper pairs. On a topological-insulator surface, corresponding to the spin polarization of exterior Majorana state, the odd-frequency Cooper pairs are fully spin polarized as well. For a Rashba superconductor, on the other hand, the spin of odd-frequency pairs is not polarized.

We have also shown that energy dependence of the local density of states around the exterior Majorana state strongly depends on the chemical potential. When the chemical potential is not sufficiently small, continuum states come close to the Fermi level because of the energy shift due to an external magnetic field. As a result, fine-tuning of the chemical potential is necessary to experimentally observe the position shift of exterior Majorana states.

ACKNOWLEDGMENTS

The authors would like to thank S. Kashiwaya and S. Tamura for useful discussions. This work was supported by JST-CREST (Grant No. JPMJCR16F2), and JSPS KAKENHI Grants No. JP16H00989 and No. JP15K17726. Y. T. is supported by a Grant-in-Aid for Scientific Research on Innovative Areas ‘‘Topological Materials Science’’ (KAKENHI Grant No. JP15H05853) from JSPS of Japan, a Grant-in-Aid for Scientific Research B (Grant No. JP15H03686), a Grant-in-Aid for Challenging Exploratory Research (Grant No. JP15K13498) from the Ministry of Educa-

tion, Culture, Sports, Science, and Technology, Japan (MEXT); Japan-RFBR JSPS Bilateral Joint Research Projects/Seminars.

Appendix A: Hamiltonian for a superconductor/topological insulator hybrid system in terms of the Bessel functions

In rotational-symmetric systems, the solutions can be well described in terms of the Bessel functions^{54,56}. We thus introduce the Bessel functions as the basis for the real space as

$$\Psi_{\mu}(\rho) = \sum_{j=1}^{j_{\max}} \begin{pmatrix} \psi_{\uparrow,\mu,j} \phi_{\mu--,j}(\alpha_{\mu--,j}\rho/R_c) \\ \psi_{\downarrow,\mu,j} \phi_{\mu-,j}(\alpha_{\mu-,j}\rho/R_c) \\ \psi_{\uparrow,\mu,j}^{\dagger} \phi_{\mu+,j}(\alpha_{\mu+,j}\rho/R_c) \\ \psi_{\downarrow,\mu,j}^{\dagger} \phi_{\mu++,j}(\alpha_{\mu++,j}\rho/R_c) \end{pmatrix}, \quad (\text{A1})$$

where we define $\mu_{s_3 s_4} = (2\mu + s_3 \ell + s_4 1)/2$, ($s_3, s_4 = \pm$) and

$$\phi_{\mu,j} = \frac{\sqrt{2}}{R_c J_{\mu+1}(\alpha_{\mu,j})} J_{\mu} \left(\alpha_{\mu,j} \frac{\rho}{R_c} \right), \quad (\text{A2})$$

with $J_{\mu}(\rho)$ being the Bessel functions with the order μ , and $\alpha_{\mu,j}$ is the j -th zero of J_{μ} . These functions $\phi_{\mu,j}$ satisfy

$$\int_0^{R_c} \phi_{\mu,j} \left(\alpha_{\mu,j} \frac{\rho}{R_c} \right) \phi_{\mu,j'} \left(\alpha_{\mu,j'} \frac{\rho}{R_c} \right) \rho d\rho = \delta_{jj'}, \quad (\text{A3})$$

where we have used $\int_0^{R_c} [J_{\mu}(\alpha_{\mu,j}\rho/R_c)]^2 \rho d\rho = [R_c J_{\mu+1}(\alpha_{\mu,j})]^2 / 2$.

In the numerical calculations, we introduce the cut-off in the summation of j . The maximum value is denoted by j_{\max} , and it is set to $j_{\max} = 200$ for the TI surface. We assume the magnetic field is spatially homogeneous $H_z(\rho) = (\nabla \times \mathbf{A})_z = H_z^{\text{ext}}$. This magnetic field can be described by the vector potential $A_{\phi} = H_z^{\text{ext}} \rho / 2$ ($H_z = [\partial_{\rho}(\rho A_{\phi})] / \rho$). We adopt the vector potential $\tilde{A}_{\phi} = S \rho / (2\ell_B^2)$ where $\ell_B = (\hbar c / |e H_z^{\text{ext}}|)^{1/2}$ is the magnetic length and $S = \text{sgn}[H_z^{\text{ext}}]$. With this basis, the Hamiltonian becomes

$$\begin{aligned}
\mathcal{H} = & \sum_{\mu} \sum_{i,j} \left(\psi_{\uparrow,\mu,i}^{\dagger} \psi_{\downarrow,\mu,i}^{\dagger} \psi_{\uparrow,\mu,i} \psi_{\downarrow,\mu,i} \right) \check{U}_1^{\dagger} \\
& \times \begin{bmatrix} M_{ij}^{(\mu--)} - \mu_F \delta_{i,j} & \hbar v_F \left(K_{\mu-,i,j}^{(-)} + A_{\mu-,i,j}^{(-)} \right) & 0 & \Delta_{\mu--, \mu+-, i,j} \\ \hbar v_F \left(K_{\mu--,i,j}^{(+)} + A_{\mu--,i,j}^{(+)} \right) & -M_{ij}^{(\mu-+)} - \mu_F \delta_{i,j} & -\Delta_{\mu-, \mu++, i,j} & 0 \\ 0 & -\Delta_{\mu++, \mu--, i,j} & -M_{ij}^{(\mu++)} + \mu_F \delta_{i,j} & \hbar v_F \left(K_{\mu+-, i,j}^{(+)} - A_{\mu+-, i,j}^{(+)} \right) \\ \Delta_{\mu+-, \mu--, i,j} & 0 & \hbar v_F \left(K_{\mu++, i,j}^{(-)} - A_{\mu++, i,j}^{(-)} \right) & M_{ij}^{(\mu+-)} + \mu_F \delta_{i,j} \end{bmatrix} \\
& \times \check{U}_1 \left(\psi_{\uparrow,\mu,j} \psi_{\downarrow,\mu,j} \psi_{\uparrow,\mu,j}^{\dagger} \psi_{\downarrow,\mu,j}^{\dagger} \right)^{\text{T}}, \tag{A4}
\end{aligned}$$

where $\check{U}_1 = \text{diag} [e^{i\pi/4} \ e^{-i\pi/4} \ e^{-i\pi/4} \ e^{i\pi/4}]$. The each term is described as

$$K_{\mu,i,j}^{(+)} = \int_0^{R_c} \frac{\alpha_{\mu,j}}{R_c} \frac{2}{R_c^2} \frac{J_{\mu+1}(\alpha_{\mu+1,i}\rho/R_c)}{J_{\mu+2}(\alpha_{\mu+1,i})} \frac{J_{\mu+1}(\alpha_{\mu,j}\rho/R_c)}{J_{\mu+1}(\alpha_{\mu,j})} \rho d\rho, \tag{A5}$$

$$K_{\mu,i,j}^{(-)} = \int_0^{R_c} \frac{\alpha_{\mu,j}}{R_c} \frac{2}{R_c^2} \frac{J_{\mu-1}(\alpha_{\mu-1,i}\rho/R_c)}{J_{\mu}(\alpha_{\mu-1,i})} \frac{J_{\mu-1}(\alpha_{\mu}\rho/R_c)}{J_{\mu+1}(\alpha_{\mu})} \rho d\rho, \tag{A6}$$

$$A_{\mu,i,j}^{(+)} = \int_0^{R_c} \frac{\mathcal{S}}{2\ell_B^2} \phi_{\mu+1}(\alpha_{\mu+1,i}\rho/R_c) \phi_{\mu}(\alpha_{\mu,j}\rho/R_c) \rho^2 d\rho, \tag{A7}$$

$$A_{\mu,i,j}^{(-)} = \int_0^{R_c} \frac{\mathcal{S}}{2\ell_B^2} \phi_{\mu-1}(\alpha_{\mu-1,i}\rho/R_c) \phi_{\mu}(\alpha_{\mu,j}\rho/R_c) \rho^2 d\rho, \tag{A8}$$

$$\Delta_{u,v,i,j} = \int_0^{R_c} \Delta(\rho) \phi_u(\alpha_{u,i}\rho/R_c) \phi_v(\alpha_{v,j}\rho/R_c) \rho d\rho, \tag{A9}$$

$$M_{ij}^{(\mu)} = \int_0^{R_c} M(\rho) \phi_{\mu}(\alpha_{\mu,i}\rho/R_c) \phi_{\mu}(\alpha_{\mu,j}\rho/R_c) \rho d\rho. \tag{A10}$$

We diagonalize numerically this $4j_{\text{max}} \times 4j_{\text{max}}$ Hamiltonian for each μ , and obtain the eigenfunction $\Phi_{\mu,\nu}$ and the energy eigenvalue $E_{\mu,\nu}$.

Appendix B: Hamiltonian for a Rashba SC in terms of the Bessel functions

Introducing the Bessel functions, the Hamiltonian for the Rashba SC becomes

$$\begin{aligned}
\mathcal{H} = & \sum_{\mu} \sum_{i,j} \left[\psi_{\uparrow,\mu,i}^{\dagger} \psi_{\downarrow,\mu,i}^{\dagger} \psi_{\uparrow,\mu,i} \psi_{\downarrow,\mu,i} \right] \\
& \times \begin{bmatrix} C_{\mu--,i,j}^{(-+)} + D_{\mu--,i,j} & \lambda \left(K_{\mu-,i,j}^{(-)} + A_{\mu-,i,j}^{(-)} \right) & 0 & \Delta_{\mu--, \mu+-, i,j} \\ \lambda \left(K_{\mu--,i,j}^{(+)} + A_{\mu--,i,j}^{(+)} \right) & C_{\mu+,i,j}^{(--)} + D_{\mu+,i,j} & -\Delta_{\mu-, \mu++, i,j} & 0 \\ 0 & -\Delta_{\mu++, \mu--, i,j} & -C_{\mu++,i,j}^{(++)} - D_{\mu++,i,j} & \lambda \left(K_{\mu+-, i,j}^{(+)} - A_{\mu+-, i,j}^{(+)} \right) \\ \Delta_{\mu+-, \mu--, i,j} & 0 & \lambda \left(K_{\mu++, i,j}^{(-)} - A_{\mu++, i,j}^{(-)} \right) & -C_{\mu+-, i,j}^{(+-)} - D_{\mu+-, i,j} \end{bmatrix} \\
& \times \left[\psi_{\uparrow,\mu,j} \psi_{\downarrow,\mu,j} \psi_{\uparrow,\mu,j}^{\dagger} \psi_{\downarrow,\mu,j}^{\dagger} \right]^{\text{T}}, \tag{B1}
\end{aligned}$$

where

$$C_{\mu,i,j}^{(\pm\pm)} = \varepsilon_{\mu,i,j}^{\pm} \pm M_0 \delta_{i,j}, \quad (\text{B2})$$

$$\varepsilon_{\mu,i,j}^{\pm} = \left[\frac{\hbar^2}{2m} \left(\frac{\alpha_{\mu,i}^2}{R_c^2} \pm \frac{\mu}{2\ell_B^2} \right) - \mu_F \right] \delta_{ij}, \quad (\text{B3})$$

$$D_{\mu,i,j} = \int_0^{R_c} \frac{\hbar^2}{2m} \frac{\rho^3}{4\ell_B^4} \phi_{\mu}(\alpha_{\mu,i}\rho/R_c) \phi_{\mu}(\alpha_{\mu,j}\rho/R_c) d\rho. \quad (\text{B4})$$

The first sign in the superscript of $C_{\mu,i,j}^{(\pm\pm)}$ corresponds to the sign in the superscript of ε , and the second one does to the sign in front of M_0 .

In the numerical calculation for the Rashba SC, j_{\max} is set to $j_{\max} = 200$. Diagonalizing the Hamiltonian for each μ , we obtain the eigenfunction $\Phi_{\mu,\nu}$ and the energy eigenvalue $E_{\mu,\nu}$.

Appendix C: Landau levels

1. Non-relativistic particle

A non-relativistic particle has a quadratic dispersion relation. The Hamiltonian is given by

$$\hat{h}_{\text{NR}} = \left[\frac{1}{2m_0} (\tilde{p}_x^2 + \tilde{p}_y^2) - \mu_F \right] \hat{\sigma}_0, \quad (\text{C1})$$

where $\tilde{\mathbf{p}} = \mathbf{p} - e\mathbf{A}/c$ and the basis is taken as $\boldsymbol{\psi}(\mathbf{r}) = [\psi_{\uparrow}(\mathbf{r}) \ \psi_{\downarrow}(\mathbf{r})]^T$. It is convenient to introduce the ladder operators a and a^{\dagger} given by

$$a = \frac{\ell_B}{\sqrt{2}\hbar} (\tilde{p}_x - i\mathcal{S}\tilde{p}_y), \quad a^{\dagger} = \frac{\ell_B}{\sqrt{2}\hbar} (\tilde{p}_x + i\mathcal{S}\tilde{p}_y), \quad (\text{C2})$$

where $\mathcal{S} = \text{sgn}[H_z^{\text{ext}}]$ and the ladder operators satisfy $[a, a^{\dagger}]_{-} = 1$. With these operators, the Hamiltonian reduces to

$$\hat{h}_{\text{NR}} = \left[\hbar\omega_c \left(a^{\dagger}a + \frac{1}{2} \right) - \mu_F \right] \hat{\sigma}_0, \quad (\text{C3})$$

where $\omega_c = |eH_z^{\text{ext}}|/mc$, and the energy eigenvalue are given by

$$E_n^{\text{NR}} = \hbar\omega_c \left(n + \frac{1}{2} \right) - \mu_F, \quad (\text{C4})$$

with $n \geq 0$ being an integer. The corresponding eigenstates are doubly degenerate and given by

$$\begin{bmatrix} |n\rangle \\ 0 \end{bmatrix}, \quad \begin{bmatrix} 0 \\ |n\rangle \end{bmatrix}, \quad (\text{C5})$$

where $|n\rangle$ is a number eigenstate satisfying the relations $a^{\dagger}a|n\rangle = n|n\rangle$, $\langle n|n'\rangle = \delta_{nn'}$, $a^{\dagger}|n\rangle = \sqrt{n+1}|n+1\rangle$, $a|n\rangle = \sqrt{n}|n-1\rangle$, and $a|0\rangle = 0$.

2. Relativistic particle

A relativistic particle has a linear dispersion relation with the Hamiltonian given by

$$\hat{h}_{\text{R}} = v_F \hat{\boldsymbol{\sigma}} \cdot \tilde{\mathbf{p}} - \mu_F = \hat{h}'_{\text{R}} - \mu_F, \quad (\text{C6})$$

where $\hat{h}'_{\text{R}} = v_F \hat{\boldsymbol{\sigma}} \cdot \tilde{\mathbf{p}}$. The 2×2 matrix form of \hat{h}'_{R} for $\mathcal{S} = +1$ is given by

$$\hat{h}'_{\text{R}} = v_F \begin{bmatrix} 0 & \tilde{p}_x - i\tilde{p}_y \\ \tilde{p}_x + i\tilde{p}_y & 0 \end{bmatrix} = \frac{\sqrt{2}\hbar v_F}{\ell_B} \begin{bmatrix} 0 & a \\ a^{\dagger} & 0 \end{bmatrix}, \quad (\text{C7})$$

where a and a^{\dagger} are defined in Eq. (C2). Using the fact that $(\hat{h}'_{\text{R}})^2$ is diagonal:

$$[\hat{h}'_{\text{R}}]^2 = 2 \left(\frac{\hbar v_F}{\ell_B} \right)^2 \begin{bmatrix} a^{\dagger}a + 1 & 0 \\ 0 & a^{\dagger}a \end{bmatrix}, \quad (\text{C8})$$

the eigenvalues of \hat{h}_{R} are given by

$$E_{\pm,n}^{\text{R}} = \pm \frac{\hbar v_F}{\ell_B} \sqrt{2n} - \mu_F, \quad (\text{C9})$$

where n is a non-negative integer.

The eigenfunctions associated with $E_{\pm,n \neq 0}^{\text{R}}$ are given by

$$\begin{bmatrix} B_{\uparrow,\pm,n} \\ B_{\downarrow,\pm,n} \end{bmatrix} = \frac{1}{\sqrt{2}} \begin{bmatrix} |n-1\rangle \\ \pm |n\rangle \end{bmatrix}, \quad (\text{C10})$$

and that with $E_{n=0}^{\text{R}}$ is

$$\begin{bmatrix} B_{\uparrow,n=0} \\ B_{\downarrow,n=0} \end{bmatrix} = \begin{bmatrix} 0 \\ |0\rangle \end{bmatrix}. \quad (\text{C11})$$

Note that the $n = 0$ state is fully spin-polarized.

Having done the same calculation for $\mathcal{S} = -1$, we can obtain the eigenfunction with $E_{\pm,n \neq 0}^{\text{R}}$ are given by

$$\begin{bmatrix} C_{\uparrow,\pm,n} \\ C_{\downarrow,\pm,n} \end{bmatrix} = \frac{1}{\sqrt{2}} \begin{bmatrix} \pm |n\rangle \\ |n-1\rangle \end{bmatrix}, \quad (\text{C12})$$

and that with $E_{n=0}^{\text{R}}$ is

$$\begin{bmatrix} C_{\uparrow,n=0} \\ C_{\downarrow,n=0} \end{bmatrix} = \begin{bmatrix} |0\rangle \\ 0 \end{bmatrix}. \quad (\text{C13})$$

Therefore, we can see that the direction of the polarized spin for $n = 0$ state is determined by \mathcal{S} .

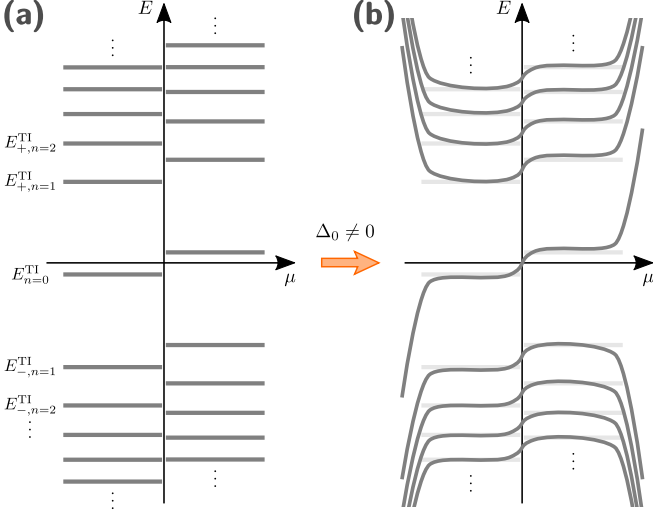


FIG. 13. Schematics of Landau levels for relativistic particles. (a) Landau levels in the normal state ($\Delta_0 = 0$) for $\mathcal{S} = \text{sgn}[H_z^{\text{ext}}] = +1$, where the particle (hole) branches $E = E_{\pm,n}^{\text{R}}(-E_{\pm,n}^{\text{R}})$ arise in the negative (positive) angular momentum μ region. (b) In the presence of superconducting pairing ($\Delta_0 \neq 0$), the Landau levels in (a) are smoothly connected. The effect of the finite system size is also taken into account in (b).

3. Angular momentum

In general, the Landau levels are degenerate with respect to the center coordinate of the cyclotron motion. The center of the orbit (X, Y) is given by

$$X = x - \mathcal{S} \frac{\ell_B^2}{\hbar} \tilde{p}_y, \quad Y = y + \mathcal{S} \frac{\ell_B^2}{\hbar} \tilde{p}_x, \quad (\text{C14})$$

By using X and Y , we can introduce another ladder operators as

$$b = \frac{1}{\sqrt{2}\ell_B}(X + i\mathcal{S}Y), \quad b^\dagger = \frac{1}{\sqrt{2}\ell_B}(X - i\mathcal{S}Y), \quad (\text{C15})$$

which satisfy $[b, b^\dagger]_- = 1$. The quantum states in the same Landau level are specified in terms of the eigenvalue of $b^\dagger b$ as

$$b^\dagger b |n, m\rangle = m |n, m\rangle, \quad (\text{C16})$$

where m is a non-negative integer. The angular momentum operator is expressed by using b and b^\dagger as

$$L_z = (\mathbf{r} \times \mathbf{p})_z, \quad (\text{C17})$$

$$= \mathcal{S} \left[\frac{\ell_B^2}{2\hbar} (\tilde{p}_x^2 + \tilde{p}_y^2) - \frac{\hbar}{2\ell_B^2} (X^2 + Y^2) \right], \quad (\text{C18})$$

$$= \mathcal{S}\hbar(a^\dagger a - b^\dagger b). \quad (\text{C19})$$

That means a quantum state $|n, m\rangle$ has the angular momentum $L_z = \mathcal{S}\hbar(n-m)$. Since n and m are non-negative integer, the angular momentum of the $|n=0, m\rangle$ states is restricted in $L_z < 0$ for $\mathcal{S} = +1$ and $L_z > 0$ for $\mathcal{S} = -1$.

4. Bogoliubov-de Gennes formalism

In the BdG formalism, the single-hole Hamiltonian $-\hat{h}_{\text{R}}^*(\mathbf{r})$ is derived by “copying” the single-particle Hamiltonian $\hat{h}_{\text{R}}(\mathbf{r})$. The BdG Hamiltonian can be described as

$$\check{H}_B = \begin{bmatrix} \hat{h}_{\text{R}} & \Delta_0 i\hat{\sigma}_2 \\ -\Delta_0 i\hat{\sigma}_2 & -\hat{h}_{\text{R}}^* \end{bmatrix}. \quad (\text{C20})$$

In the normal state (i.e., $\Delta_0 = 0$), the energy eigenvalues of \check{H}_B are given by $\pm E_{\pm,n}^{\text{R}}$ as shown schematically in Fig. 13(a). In the superconducting state, the energy spectrum is modified by the pair potential Δ_0 as shown in Fig. 13(b), which is drawn for $\mathcal{S} = +1$. For the case of $\mathcal{S} = -1$, the particle (hole) branches arises in $\mu > 0$ ($\mu < 0$), and hence, the sign of the slope of the chiral Majorana mode at $\mu = 0$ becomes opposite.

¹ X.-L. Qi and S.-C. Zhang, Rev. Mod. Phys. **83**, 1057 (2011).

² Y. Tanaka, M. Sato, and N. Nagaosa, J. Phys. Soc. Jpn. **81**, 0111013 (2012).

³ C. W. J. Beenakker, Annu. Rev. Condens. Matter Phys. **4**, 113 (2013).

⁴ M. Sato and Y. Ando, Reports on Progress in Physics **80**, 076501 (2017).

⁵ N. Read and D. Green, Phys. Rev. B **61**, 10267 (2000).

⁶ D. A. Ivanov, Phys. Rev. Lett. **86**, 268 (2001).

⁷ J. Nilsson, A. R. Akhmerov, and C. W. J. Beenakker, Phys. Rev. Lett. **101**, 120403 (2008).

⁸ F. Wilczek, Nature Phys. **5**, 614 (2009).

⁹ K. T. Law, P. A. Lee, and T. K. Ng, Phys. Rev. Lett. **103**, 237001 (2009).

¹⁰ J. Alicea, Y. Oreg, G. Refael, F. von Oppen, and M. Fisher, Nature Physics **7**, 412 (2011).

¹¹ M. Leijnse and K. Flensberg, Semiconductor Science and Technology **27**, 124003 (2012).

¹² J. Alicea, Rep. Prog. Phys. **75**, 076501 (2012).

- ¹³ S. R. Elliott and M. Franz, *Rev. Mod. Phys.* **87**, 137 (2015).
- ¹⁴ M. Sato and S. Fujimoto, *Journal of the Physical Society of Japan* **85**, 072001 (2016).
- ¹⁵ M. Hell, M. Leijnse, and K. Flensberg, *Phys. Rev. Lett.* **118**, 107701 (2017).
- ¹⁶ J. Cayao, P. San-Jose, A. M. Black-Schaffer, R. Aguado, and E. Prada, *Phys. Rev. B* **96**, 205425 (2017).
- ¹⁷ R. Lutchyn, E. Bakkers, L. Kouwenhoven, P. Krogstrup, C. Marcus, and Y. Oreg, [arXiv:1707.04899](https://arxiv.org/abs/1707.04899).
- ¹⁸ R. Aguado, *Riv. Nuovo Cimento* **40**, 523 (2017).
- ¹⁹ A. Kitaev, *Ann. Phys.* **303**, 2 (2003).
- ²⁰ C. Nayak, S. H. Simon, A. Stern, M. Freedman, and S. Das Sarma, *Rev. Mod. Phys.* **80**, 1083 (2008).
- ²¹ A. Y. Kitaev, *Usp. Fiz. Nauk (Suppl.)* **171**, 131 (2001).
- ²² M. Sato, Y. Takahashi, and S. Fujimoto, *Phys. Rev. Lett.* **103**, 020401 (2009).
- ²³ Y. Oreg, G. Refael, and F. von Oppen, *Phys. Rev. Lett.* **105**, 177002 (2010).
- ²⁴ R. M. Lutchyn, J. D. Sau, and S. Das Sarma, *Phys. Rev. Lett.* **105**, 077001 (2010).
- ²⁵ J. D. Sau, R. M. Lutchyn, S. Tewari, and S. Das Sarma, *Phys. Rev. Lett.* **104**, 040502 (2010).
- ²⁶ J. Alicea, *Phys. Rev. B* **81**, 125318 (2010).
- ²⁷ S. Nakosai, Y. Tanaka, and N. Nagaosa, *Phys. Rev. Lett.* **108**, 147003 (2012).
- ²⁸ A. Yamakage, Y. Tanaka, and N. Nagaosa, *Phys. Rev. Lett.* **108**, 087003 (2012).
- ²⁹ K. Björnson and A. M. Black-Schaffer, *Phys. Rev. B* **88**, 024501 (2013).
- ³⁰ V. Mourik, K. Zuo, S. Frolov, E. P. A. M. Bakkers, S. Plissard, and L. P. Kouwenhoven, *Science* **336**, 1003 (2012).
- ³¹ M. Deng, C. Yu, G. Huang, M. Larsson, P. Caroff, and H. Xu, *Nano Lett.* **12**, 6414 (2012).
- ³² L. Rokhinson, X. Liu, and J. Furdyna, *Nat. Phys.* **8**, 795 (2012).
- ³³ A. Das, Y. Ronen, Y. Most, Y. Oreg, and M. H. H. Shtrikman, *Nature Phys.* **8**, 887 (2012).
- ³⁴ S. Nadj-Perge, I. K. Drozdov, J. Li, H. Chen, S. Jeon, J. Seo, A. H. MacDonald, B. Bernevig, and A. Yazdani, *Science* **346**, 602 (2014).
- ³⁵ I. van Weperen, B. Tarasinski, D. Eeltink, V. S. Pribiag, S. R. Plissard, E. P. A. M. Bakkers, L. P. Kouwenhoven, and M. Wimmer, *Phys. Rev. B* **91**, 201413 (2015).
- ³⁶ J. Shabani, M. Kjaergaard, H. J. Suominen, Y. Kim, F. Nichele, K. Pakrouski, T. Stankevic, R. M. Lutchyn, P. Krogstrup, R. Feidenhans'l, S. Kraemer, C. Nayak, M. Troyer, C. M. Marcus, and C. J. Palmstrøm, *Phys. Rev. B* **93**, 155402 (2016).
- ³⁷ J. Chen, P. Yu, J. Stenger, M. Hocevar, D. Car, S. R. Plissard, E. P. Bakkers, T. D. Stanescu, and S. M. Frolov, [arXiv:1610.04555](https://arxiv.org/abs/1610.04555) (2016).
- ³⁸ M. T. Deng, S. Vaitiekenas, E. B. Hansen, J. Danon, M. Leijnse, K. Flensberg, J. Nygård, P. Krogstrup, and C. M. Marcus, *Science* **354**, 1557 (2016).
- ³⁹ R. Pawlak, M. Kisiel, J. Klinovaja, T. Meier, S. Kawai, T. Glatzel, D. Loss, and E. Meyer, *npj Quantum Information* **2**, 16035 (2016).
- ⁴⁰ F. Nichele, A. C. C. Drachmann, A. M. Whiticar, E. C. T. O'Farrell, H. J. Suominen, A. Fornieri, T. Wang, G. C. Gardner, C. Thomas, A. T. Hatke, P. Krogstrup, M. J. Manfra, K. Flensberg, and C. M. Marcus, *Phys. Rev. Lett.* **119**, 136803 (2017).
- ⁴¹ H. J. Suominen, M. Kjaergaard, A. R. Hamilton, J. Shabani, C. J. Palmstrøm, C. M. Marcus, and F. Nichele, *Phys. Rev. Lett.* **119**, 176805 (2017).
- ⁴² R. S. Deacon, J. Wiedenmann, E. Bocquillon, F. Domínguez, T. M. Klapwijk, P. Leubner, C. Brüne, E. M. Hankiewicz, S. Tarucha, K. Ishibashi, H. Buhmann, and L. W. Molenkamp, *Phys. Rev. X* **7**, 021011 (2017).
- ⁴³ J. E. Sestoft, T. Kanne, A. N. Gejl, [et al.](https://arxiv.org/abs/1711.06864), [arXiv:1711.06864](https://arxiv.org/abs/1711.06864) (2017).
- ⁴⁴ Ö. Gül, H. Zhang, J. D. Bommer, M. W. de Moor, D. Car, S. R. Plissard, E. P. Bakkers, A. Geresdi, K. Watanabe, T. Taniguchi, and L. P. Kouwenhoven, *Nature nanotechnology* **13**, 192 (2018).
- ⁴⁵ L. Fu and C. L. Kane, *Phys. Rev. Lett.* **100**, 096407 (2008).
- ⁴⁶ L. Fu and C. L. Kane, *Phys. Rev. Lett.* **102**, 216403 (2009).
- ⁴⁷ Y. Tanaka, T. Yokoyama, and N. Nagaosa, *Phys. Rev. Lett.* **103**, 107002 (2009).
- ⁴⁸ A. R. Akhmerov, J. Nilsson, and C. W. J. Beenakker, *Phys. Rev. Lett.* **102**, 216404 (2009).
- ⁴⁹ J. D. Sau, R. M. Lutchyn, S. Tewari, and S. Das Sarma, *Phys. Rev. B* **82**, 094522 (2010).
- ⁵⁰ P. A. Iosevich and M. V. Feigel'man, *Phys. Rev. Lett.* **106**, 077003 (2011).
- ⁵¹ M. Veldhorst, M. Snelder, M. Hoek, T. Gang, V. K. Guduru, X. L. Wang, U. Zeitler, W. G. van der Wiel, A. A. Golubov, H. Hilgenkamp, and A. Brinkman, *Nat. Mat.* **11**, 417 (2012).
- ⁵² J. R. Williams, A. J. Bestwick, P. Gallagher, S. S. Hong, Y. Cui, A. S. Bleich, J. G. Analytis, I. R. Fisher, and D. Goldhaber-Gordon, *Phys. Rev. Lett.* **109**, 056803 (2012).
- ⁵³ C. Chamon, R. Jackiw, Y. Nishida, S.-Y. Pi, and L. Santos, *Phys. Rev. B* **81**, 224515 (2010).
- ⁵⁴ M. Cheng, R. M. Lutchyn, V. Galitski, and S. Das Sarma, *Phys. Rev. B* **82**, 094504 (2010).
- ⁵⁵ A. L. Rakhmanov, A. V. Rozhkov, and F. Nori, *Phys. Rev. B* **84**, 075141 (2011).
- ⁵⁶ T. Kawakami and X. Hu, *Phys. Rev. Lett.* **115**, 177001 (2015).
- ⁵⁷ R. S. Akzyanov, A. L. Rakhmanov, A. V. Rozhkov, and F. Nori, *Phys. Rev. B* **92**, 075432 (2015).
- ⁵⁸ R. S. Akzyanov, A. L. Rakhmanov, A. V. Rozhkov, and F. Nori, *Phys. Rev. B* **94**, 125428 (2016).
- ⁵⁹ J.-P. Xu, M.-X. Wang, Z. L. Liu, J.-F. Ge, X. Yang, C. Liu, Z. A. Xu, D. Guan, C. L. Gao, D. Qian, Y. Liu, Q.-H. Wang, F.-C. Zhang, Q.-K. Xue, and J.-F. Jia, *Phys. Rev. Lett.* **114**, 017001 (2015).
- ⁶⁰ Y. Tanaka and A. A. Golubov, *Phys. Rev. Lett.* **98**, 037003 (2007).
- ⁶¹ Y. Tanaka, A. A. Golubov, S. Kashiwaya, and M. Ueda, *Phys. Rev. Lett.* **99**, 037005 (2007).
- ⁶² Y. Tanaka, Y. Tanuma, and A. A. Golubov, *Phys. Rev. B* **76**, 054522 (2007).
- ⁶³ Y. Asano, Y. Tanaka, and A. A. Golubov, *Phys. Rev. Lett.* **98**, 107002 (2007).
- ⁶⁴ M. Eschrig and T. Löfwander, *Nature Physics* **4**, 138 (2008).
- ⁶⁵ T. Yokoyama, Y. Tanaka, and A. A. Golubov, *Phys. Rev. B* **78**, 012508 (2008).
- ⁶⁶ Y. Tanuma, N. Hayashi, Y. Tanaka, and A. A. Golubov, *Phys. Rev. Lett.* **102**, 117003 (2009).
- ⁶⁷ Y. Asano, A. A. Golubov, Y. V. Fominov, and Y. Tanaka, *Phys. Rev. Lett.* **107**, 087001 (2011).

- ⁶⁸ T. Daino, M. Ichioka, T. Mizushima, and Y. Tanaka, *Phys. Rev. B* **86**, 064512 (2012).
- ⁶⁹ Y. Asano and Y. Tanaka, *Phys. Rev. B* **87**, 104513 (2013).
- ⁷⁰ S. Higashitani, H. Takeuchi, S. Matsuo, Y. Nagato, and K. Nagai, *Phys. Rev. Lett.* **110**, 175301 (2013).
- ⁷¹ S.-I. Suzuki and Y. Asano, *Phys. Rev. B* **89**, 184508 (2014).
- ⁷² S.-I. Suzuki and Y. Asano, *Phys. Rev. B* **94**, 155302 (2016).
- ⁷³ M. Alidoust, A. Zyuzin, and K. Halterman, *Phys. Rev. B* **95**, 045115 (2017).
- ⁷⁴ O. Kashuba, B. Sothmann, P. Buset, and B. Trauzettel, *Phys. Rev. B* **95**, 174516 (2017).
- ⁷⁵ J. Linder and A. V. Balatsky, [arXiv:1709.03986](https://arxiv.org/abs/1709.03986) (2017).
- ⁷⁶ V. Stanev and V. Galitski, *Phys. Rev. B* **89**, 174521 (2014).
- ⁷⁷ A. M. Black-Schaffer and A. V. Balatsky, *Phys. Rev. B* **87**, 220506 (2013).
- ⁷⁸ S.-I. Suzuki and Y. Asano, *Phys. Rev. B* **91**, 214510 (2015).
- ⁷⁹ X. Liu, J. D. Sau, and S. Das Sarma, *Phys. Rev. B* **92**, 014513 (2015).
- ⁸⁰ H. Ebisu, K. Yada, H. Kasai, and Y. Tanaka, *Phys. Rev. B* **91**, 054518 (2015).
- ⁸¹ K. Björnson and A. M. Black-Schaffer, *Phys. Rev. B* **91**, 214514 (2015).
- ⁸² H. Ebisu, B. Lu, K. Taguchi, A. A. Golubov, and Y. Tanaka, *Phys. Rev. B* **93**, 024509 (2016).
- ⁸³ H. Ebisu, B. Lu, J. Klinovaja, and Y. Tanaka, *Progress of Theoretical and Experimental Physics* **2016**, 083I01 (2016).
- ⁸⁴ J. Cayao and A. M. Black-Schaffer, *Phys. Rev. B* **96**, 155426 (2017).
- ⁸⁵ D. Kuzmanovski and A. M. Black-Schaffer, *Phys. Rev. B* **96**, 174509 (2017).
- ⁸⁶ J. W. McClure, *Phys. Rev.* **104**, 666 (1956).
- ⁸⁷ A. Luican, G. Li, and E. Y. Andrei, *Phys. Rev. B* **83**, 041405 (2011).
- ⁸⁸ M. O. Goerbig, *Rev. Mod. Phys.* **83**, 1193 (2011).
- ⁸⁹ An exterior Majorana bound state is reported also in superconducting systems with magnetic skyrmions. See G. Yang, P. Stano, J. Klinovaja, and D. Loss, *Phys. Rev. B* **93**, 224505 (2016).
- ⁹⁰ The condition obtained here is different from that derived in Ref. 58, which discusses the condition for the energy gap due to the hybridization between vortex and exterior MBSs to be zero or small enough.
- ⁹¹ We also calculate the spin density of the whole system (not shown), and find that it is almost unpolarized since the contribution from the exterior MBS is negligible compared with that from the continuum states. Therefore, to observe the spin-polarization of the MBS, we need a spin- and energy-resolved measurement, which can be realised by replacing a metallic STS tip by a ferromagnetic one..